A brain network basis of Fragile X syndrome behavioral penetrance determined by X chromosome inactivation in female mice

Eric Szelenyi[1,2,3], Danielle Fisenne[1,4,5], Joseph E Knox[3], Julie A Harris[3], James A Gornet[1,6] Ramesh Palaniswamy[1], Yongsoo Kim[1,7], Kannan Umadevi Venkataraju[1], Pavel Osten[1]*

[1]Cold Spring Harbor Laboratory, Cold Spring Harbor, NY.11724.
[2]Program in Neuroscience, Stony Brook University, Neurobiology and Behavior, Stony Brook, NY 11794.
[3]Allen Institute for Brain Science, Seattle, WA 98109.
[4]Hofstra University, Hempstead, NY 11549.
[5]Certerra Inc., Farmingdale, NY 11735
[6]Columbia University, New York, NY 10027
[7]College of Medicine, Penn State University, Hershey, PA 17033.
*corresponding author

ABSTRACT

X-chromosome inactivation (XCI) in females is vital for normal brain function and cognition, as many X-linked genetic mutations lead to mental retardation and autism spectrum disorders, such as the fragile X syndrome (FXS). However, the degree by which XCI regulates disease presentation has been poorly investigated. To study this regulation in the mouse, here we quantified the brainwide composition of active-XC cells at single cell resolution using an X-linked MECP2-EGFP allele with known parent-of-origin. We present evidence that whole-brains, including all regions, on average favor maternal XC-active cells by 20%, or 8 million cells. This bias was conserved in heterozygous FXS mutant mice, which also corresponded to disease penetrance in maternal but not paternal *FMR1* null mice. To localize the physical source of behavioral penetrance, brain-wide correlational screens successfully mapped mouse performance to cell densities in putative sensorimotor (e.g. sensory hindbrain, thalamus, globus pallidus) and sociability (e.g. visual/entorhinal cortices, bed nucleus stria terminalis, medial preoptic area) behavioral circuits of the open field sensorimotor and 3-chamber sociability assays, respectively. Overall, 50%/50% healthy/mutant cell density ratios in these sub-networks were required for disease presentation in each behavior. These results suggest female X-linked behavioral penetrance of disease is regulated at the distributed level of mutant cell density in behavioral circuits, which is set by XCI that is subject to parent-of-origin effects. This work provides a novel finding behind the broad and varied behavioral phenotypes commonly featured in female patients debilitated by X-linked mental disorders and may offer new entry points for behavioral therapeutics.

INTRODUCTION

X chromosome inactivation (XCI) is a process by which one of the two female X chromosomes – the maternally inherited Xm chromosome and paternally inherited Xp chromosome – is randomly chosen for transcriptional silencing through epigenetics during gastrulation of the embryo (*1, 2*). It is proposed that XCI exists as a normalizing mechanism with regard to the male XY counterpart, in which XC gene transcription originates from the only XC present, the Xm. Alternatively, XCI in females produces a mosaic, and/or zoned distribution pattern of both Xm and Xp-active cells throughout all somatic tissue.

The XC expresses more brain-specific genes than any other chromosome in both mouse and human (*3*) and many XC mutations give rise to mental disease such as X-linked mental retardation (XLMR) and autism (e.g. Fragile X syndrome [FXS]) (*4-6*). Genetic-labeling experiments have illustrated mosaic distribution patterns of active-XC (XCa) cells within the female mouse brain (*7*), which corresponds with broad and variable behaviors clinically described amongst female X-linked patients (*8*). Research in mice additionally suggests the existence of a small but notable Xm-active bias in the brain (*9-11*). However, the extent to which these and other unknown XCI brain factors play as behavioral determinants has yet to be sufficiently described. Achieving this end goal requires a quantitative approach capable of achieving cellular detection dynamically throughout the many spatial dimensions of the brain. The utility of such an approach, in combination with XCa labeling and X-linked disease mouse models holds potential to bridge XCI with the etiology of X-linked disease penetrance and behavioral traits.

RESULTS

We report the first quantitative description of cellular XCa distributions mapped throughout the whole-brain at single cell resolution. Our strategy focuses upon application of an automated whole-brain imaging and cell counting platform (*12, 13*) with female mice harboring the X-linked knock in MeCP2-EGFP fusion allele (*14-17*). We first determined the capacity of this allele to serve as an unambiguous cellular XCa reporter through immunohistochemical analyses performed amongst several brain areas of *MeCP2*$^{EGFP/EGFP}$ (i.e. Xm/Xp-active) reporter brains (**Fig. 1S1A-B**). Accordingly, we determined that approximately all cells, as identified by DAPI staining, expressed MeCP2-EGFP (mean: 95%; range: 91-98%) and 88% were stained positive with the neuronal marker NeuN (range 78-98%). Most NeuN+ cells measured also expressed MeCP2-EGFP (mean: 88%; range 82-94%). Conversely, MeCP2-EGFP+ cells colabeled with NeuN widely varied widely across the brain, with highest and lowest colocalization found in the primary somatosensory cortex (94%) and brainstem (29%), respectively. The average combined MeCP2-EGFP+/NeuN+ colocalization amongst all brain regions examined was 62%. These observations importantly cross-validate previous reports that observed heterogeneity in neuron/non-neuron cellular ratios in different brain regions, which averages out to a final 68% neuronal composition within the entire brain (*18*). Additionally, these data confirm that roughly all cell-types of the brain express MeCP2

(*19*) as indicated by the MeCP2-EGFP reporter allele's distribution. Therefore, we confidently selected this allele for use in faithful parent-of-origin-based cellular tracking of the XCa via MeCP2-EGFP cellular fluorescence.

We transmitted the MeCP2-EGFP reporter allele from both female and male breeders in order to label, quantify, and compare Xm-active or Xp-active cells, respectively, in separate groups of female offspring (**Fig. 1A**). Serial 2-photon tomography (STP)-acquired whole-brain datasets were processed at 1 um X x 1um Y x 50 um Z resolution for both Xm-active (n=18) and Xp-active (n=19) reporter mice, and Xm/Xp-active reporter mice (n=6) were additionally imaged to serve as 100% cell count controls. We further enhanced the Z resolution to 2.5 um by post-hoc application of a 2D:3D correction factor (2.6x) determined beforehand and calculated offline (**Fig. 1S2A,B**). Human experts benchmarked the performance of an automated MeCP2-EGFP+ cell detection algorithm used to process all samples (**Fig. 1S2C-E**). The composite F-score determined for the MeCP2-EGFP algorithm was 0.86, or, 86% of human expert performance.

Whole-brain quantifications revealed significantly more labeled cells (20% or 8 x 10^7) in Xm-active (median: 2.4 x 10^7; SD: 4.5 x 10^6) than Xp-active reporter mice (median: 1.6 x 10^7; SD: 5.3 x 10^6; Mann-Whitney U = 62, p = 0.0006; **Fig. 1A-C**). Xm/Xp-active reporter mice contained 3.9 x 10^7 ± 2.5 x 10^7 labeled cells (**Fig. 1C**), which replicates findings by others (*20*) as well as the combined Xm- and Xp-active reporter means quantified here (4.02 x 10^7 cells, **Fig. 1C**). Xm-active and Xp-active cell counts therefore represent a 60 and 40% composition, respectively, of the female mouse brain when expressed to either 100% control group values (i.e. Xm/Xp-active or combined heterozygous means). No change in MeCP2-EGFP+ cellular fluorescence intensity was observed amongst Xm- and Xp-active reporter groups (**Fig. 1S2F,G**), signifying that these cell count differences are bona-fide parent-of-origin effects on XCa cell choice and cannot be attributed to an artifact of the genetic reporter.

To understand if the observed whole-brain Xm-active cellular bias is retained across all ontological divisions of the brain, whole-brain cell counts were next digitally segmented into 741 regions-of-interest (ROIs; **Methods**). Cell densities for each ROI were calculated and first compared amongst reporter groups across 9 major brain divisions: isocortex, olfactory area, hippocampal formation, cortical subplate, cerebral nuclei, thalamus, hypothalamus, midbrain, and hindbrain (**Figs. 1D-G**). Accordingly, a 2-way ANOVA found a main effect of reporter group (F = 1, 315 = 125.5, p < .0001; Fig. 1D). FDR-corrected multiple comparison post-hoc tests revealed significantly greater cell densities in the Xm-active reporter group amongst all major ROIs studied (**Fig. 1D**), including the isocortex (mean ± SD; Xm-active: 7.2 x 10^4 ± 1.7 x 10^4, Xp-active: 5.1 x 10^4 ± 1.4 x 10^4 cells/mm^3; p < 0.0001), olfactory area (Xm-active: 8.2 x 10^4 ± 1.7 x 10^4, Xp-active: 6.2 x 10^4 ± 1.7 x 10^4 cells/mm^3; p < 0.0001), hippocampal formation (Xm-active: 7.0 x 10^4 ± 1.5 x 10^4, Xp-active: 5.3 x 10^4 ± 1.4 x 10^4 cells/mm^3; p = 0.0005), cortical subplate (Xm-active: 6.4 x 10^4 ± 1.4 x 10^4, Xp-active: 4.7 x 10^4 ± 1.2 x 10^4 cells/mm^3; p = 0.0003), cerebral nuclei (Xm-active: 6.9 x 10^4 ± 1.6 x 10^4, Xp-active: 5.2 x 10^4 ± 1.2 x 10^4 cells/mm^3; p = 0.0005), thalamus (Xm-active: 5.0 x 10^4 ± 1.4 x 10^4, Xp-active: 3.6 x 10^4 ± 1.2 x 10^4 cells/mm^3; p = 0.002), hypothalamus (Xm-active: 7.1 x 10^4 ± 1.4 x 10^4, Xp-active: 5.2 x 10^4 ± 1.4 x 10^4 cells/mm^3; p < 0.0001), midbrain (Xm-active: 5.7 x 10^4 ± 1.5 x 10^4, Xp-active: 3.9 x 10^4 ± 1.4 x 10^4 cells/mm^3; p = 0.0001), and

hindbrain (Xm-active: $3.0 \times 10^4 \pm 1.3 \times 10^4$, Xp-active: $1.6 \times 10^4 \pm 0.8 \times 10^4$ cells/mm^3; p = 0.0018), with average percent Xm-active/Xp-active cell density compositions being 58/42, 57/43, 58/42, 57/43, 58/42, 58/42, 60/40, and 66/34, respectively, of the homozygous reporters (data not shown). These results suggest that the whole-brain Xm-active cellular bias is evenly distributed across major subdivisions of the mouse brain. In addition, visualization and analysis of all segmented ROIs across these subdivisions allowed understanding of the percent XCa landscape for each sample (**Fig. 1S3**). This depiction displayed a conserved ROI to whole-brain percent XCa cell density, with no apparent intra-brain patterns observed (**Fig. 1S3B).** The average ROI to whole-brain difference in percent cell density across all samples and segmented ROIs was 0 (**Fig. 1S3C**), suggesting that the XCI status of all brain regions closely resembles that of it's entirety. However, 95th percentiles of individual ROI percent cell densities per sample represented a range of 15-52 cell density percent departure from the medians (**Fig. 1S3D**), and standard deviations of 8-16% around the mean (**Fig. 1S3E**). This underscores that the whole-brain to sub-region relationship of cellular XCI status is related, but not exact and/or partial to particular areas of the brain.

Because XCI defines cellular distributions of Xm- and Xp-active cells in the female brain, we next investigated how heterozygous inheritance of an X-linked mutation affects behavioral penetrance due to XCI. For this, we utilized a mouse model of FXS in which the expression of the X-linked *FMR1* gene is disrupted (*21*). To enable XCa cellular counting in behaviorally phenotyped FXS female mice, we generated double heterozygous transgenics in which healthy XCa cells reported the measurable MeCP2-EGFP allele and the reciprocal XCa cells harbored the mutant or wild-type *FMR1* allele. Swapping the parent-of-origin for each allele in separate breeding pairs allowed for simultaneous parent-of-origin comparisons (i.e. $Xm^{FMR1\ KO}/Xp^{MeCP2\text{-}EGFP}$ versus $Xm^{MeCP2\text{-}EGFP}/Xp^{FMR1\ KO}$) to be made in behavioral assessments and whole-brain XCa quantification (**Fig. 2A**). A behavioral battery consisting of the open field (OFT), T-maze, and 3-chamber tests was used to assess levels of sensorimotor performance, spatial memory, and sociability, respectively (**Fig. 2B**). Behavioral deficits were observed only in maternal ($Xm^{FMR1\ KO}/Xp^{MeCP2\text{-}EGFP}$) and not paternal ($Xm^{MeCP2\text{-}EGFP}/Xp^{FMR1\ KO}$) *FMR1* KO mice when compared with *FMR1* WT ($Xm^{FMR1WT}/Xp^{MeCP2\text{-}EGFP}$) mice. Accordingly, all genotypes traveled similar total distances in the OFT (*FMR1* WT [18.5 m ± 6.28 m]; maternal *FMR1* KO [22.62 m ± 9.71 m]; paternal *FMR1* KO [19.63 m ± 6.39 m]) (**Fig. 2C, left**). However, normalizing the center distance by total distance traveled revealed a significantly lower percent center distance traveled for maternal *FMR1* KO (9.789% ± 3.748%; U=2.309, q=0.032) and not paternal *FMR1* KO (11.9% ± 5.183%; U=33, q=0.80) mice when compared to *FMR1* WT (13.08% ± 2.165%) mice (**Fig. 2C right**). Spatial memory, as measured by percent alternation in the T-maze, was signifcantly reduced for maternal (47.67% ± 14.32%; U=12, q=0.037) but not paternal *FMR1* KO mice (53.38% ± 18.63%; U=15.5, q=0.08) when compared to *FMR1* WT mice (68.63% ± 14.11%; **Fig. 2D**). Finally, we determined mouse sociability based on time spent with stranger mice in the 3-chamber test. A 3 (percent chamber time) x 3 (genotype) within subjects two-way ANOVA analysis of percent chamber time spent revealed a significant chamber by genotype interaction (F(4,44 = 3.214, p=0.02). FDR-corrected post-hoc comparisons confirmed a significant preference for *FMR1* WT mice to spend time in the social stranger chamber (47% ± 7.4%) in comparison to center chamber (23% ± 3.9%,

q<0.001) or empty chamber (31%, ± 7.1%; q<0.001). Paternal *FMR1* KOs also showed a percent stranger chamber time preference (43% ± 6.6%) in comparison to center chamber (24% ± 7%, q<0.001) or empty chamber (33% ± 8.6%, q=0.024). Both *FMR1* WT and paternal *FMR1* KO mice significantly preferred to spend more time secondarily in the empty chamber versus center (*FMR1* WT: q=0.029; paternal *FMR1* KO: q=0.034). In contrast, maternal *FMR1* KO mice showed no chamber preferences for stranger (37% ± 7.3%; q=0.34 vs center; q=0.19 vs empty), center (33% ± 7.5%; q=0.44 versus empty), or empty chamber (30% ± 6.7%) (**Fig. 2E**). Between-subjects two-way ANOVA analysis also revealed a significantly reduced social chamber time spent for maternal *FMR1* KO mice when compared to *FMR1* WT littermates (q=0.018), and signifcantly more center chamber time when compared to both *FMR1* WT (q=0.005) and paternal *FMR1* KO (q=0.005) mice (**Fig. 2S1A**). Sniffing interactions (**Fig. 2S1B)**, amount of behavioral freezing (**Fig. 2S1C)**, and distance traveled (**Fig. 2S1D)** across chambers did not differ amongst groups, indicating a specific phenotype for maternal *FMR1* KO mice to avoid the chambers with novel objects (i.e. stranger mouse or empty cup).

Similarly to WT reporter mice, $Xm^{MeCP2\text{-}EGFP}/Xp^{FMR1\ WT}$ reporter brains contained significantly more (median: 2.4 x 10^7, SD: 4.25 x 10^6 cells/mm^3; 36%) XCa cells than $Xm^{FMR1\ WT}/Xp^{MeCP2\text{-}EGFP}$ (median: 1.65 x 10^7 cells/mm^3; SD: 5.3 x 10^6; Mann Whitney U(4) = 7; p = 0.003) (**Fig. 2S2**). This difference persisted in reciprocal *FMR1* KO comparisons, whereby $Xm^{MeCP2\text{-}EGFP}/Xp^{FMR1\ KO}$ mice contained significantly more XCa-reporting cells (median 2.55 x 10^7; SD: 4.9 x 10^4 cells/mm^3) than $Xm^{FMR1\ KO}/Xp^{MeCP2\text{-}EGFP}$ mice (median: 1.7 x 10^7; SD: 5.3 x 10^6 cells/mm3; Mann Whitney U (9); p = 0.0289) (**Fig. 2F**). When normalized by the Xm/Xp total cell density estimate, 0% paternal (left), and 75% maternal (right) *FMR1* KO brains imaged displayed >50% mutant XCa whole-brain cell density (**Fig. 2G**).

We next asked if FXS penetrance in maternal *FMR1* KO carriers could be localized to healthy cell densities existing amongst individual or combinations of brain regions. For this, we conducted brain-wide correlational screens amongst ROI-segmented, healthy XCa cell densities with behavioral scores from each behavioral assay. This analysis revealed striking brain network-related patterns of healthy cell density correlation for OFT and 3-chamber scores within maternal *FMR1* KO mice brains only (**Fig. 3A, B, E; Fig. 3S1**). Control *FMR1* WT and paternal *FMR1* KO mice both failed to elicit similar patterns of significant correlation or any ROI correlations when threshholded at p=0.01 (**Fig. 3S1**). The OFT correlated ROIs showed no convergence with those of the 3-chamber. Specifically, hindbrain and thalamic ROIs composed 50% and 34% total ROIs for OFT and 0 and 2% for 3-chamber, respectively. No cortical or hippocampal ROIs were significantly related to OFT behavior whereas 25 and 23% of ROIs in these areas were related to 3-chamber performance (**Fig. 3S1**). The majority of positive ROI healthy cell density correlations identified for OFT scores were located in thalamic (e.g. medial geniculate complex, medial [MgM]; r = 0.93, p = 0.001, ventral posterolateral nucleus [VPL]; r = 0.92, p = 0.001, and posterior limiting nucleus [POL]; r = 0.93, p = 0.001) and hindbrain (e.g. spinal nucleus of the trigeminal, oral [SPVO], r = 0.96, p = 0.0001, cochlear nucleus [CN], r = 0.93, p = 0.001, and dorsal cochlear nucleus [DCO], r = 0.93, p = 0.001) sensory regions (**Figs. 3B, E, S1**). Outside of these areas, sensorimotor integrators such as the magnocellular nucleus (MA; r = 0.91, p = 0.002) and nucleus of the diagonal band (NDB; r = 0.90, p = 0.003) located in the cerebral nuclei as

well as the ventrolateral preoptic area (VLPO; r = 0.91, p = 0.002) of the hypothalamus showed strong correlations. 3-chamber social task correlations, identified as a negative relationship with percent time spent in center chamber, revealed a separate network of ROIs collectively involved in object recognition (e.g. primary lateral visual area [VISl]; r = -0.86; p=0.006) (*22*), spatial processing (e.g. medial entorhinal area [ENTm]: r = -0.90; p=0.003 (*23*), as well as anxiety/social encoding brain regions (e.g. bed nucleus of stria terminalis [BST]: r = -0.84, p=0.009 (*24*); basolateral amygdala, primary [BLAp]: r = -0.87; p=0.005 (*25*)); medial preoptic area [MPO]: r = -0.89; p=0.002 (*26*), molecular layer of the dentate gyrus [DGmo]: r = -0.86; p=0.006 (*27*)) (**Figs. 3B, E; S1**).

We hypothesized that the shared and related behavioral function of correlated ROIs demonstrates the presence of structural connectivity, or behavioral circuitry underlying FXS behavioral penetrance. For this purpose, normalized connection densities of OFT and 3-chamber correlated ROI networks were calculated using a structural connectivity matrix (*28*) (Knox et al, In-press). We tested for the presence of structural connectivity by comparing these experimental median values against those obtained from 1000 randomly sampled networks of the same ROI amount and total inter-ROI distance (**Methods; Fig. 3C-D, F-G**). Median normalized connection densities for OFT (1.2×10^{-5}) (**Fig. 3C-D**) and 3-chamber (1.1×10^{-4}) (**Fig. F-G**) ROI networks were both significantly stronger than the matching randomly sampled networks (OFT sample network density = 7.1×10^{-6}; p = 6.2×10^{-261}; 3-chamber sample network density = 7.1×10^{-6}; p = 0.0). The experimental ROI network connectivity densities fell in the 93rd (OFT) and 100th (3-chamber) percentiles of each sample network's distribution, thereby indicating that the networks exist as structurally connected sub-networks in the mouse brain.

To understand if behavioral performance can be predicted by healthy cell density defined specifically within the connectivity-defined behavioral networks, healthy cell density percent for each behavioral network of ROIs were next calculated and regressed against behavioral performance for each genotype (**Fig. 4 A, D**). ROI network healthy cell density percent was found to be a significant predictor of mouse behavioral performance for maternal *FMR1* KO mice in both OFT (F (1,6) = 21.55; p = 0.004, r^2 = 0.78) and 3-chamber assays (F (1,6) = 18.97; p = 0.005, r^2 = 0.76) (**Fig. 4 A, D center**). Conversely, control *FMR1* WT and paternal *FMR1* KO ROI network percent cell density percent both failed to signifcantly predict OFT (*FMR1* WT: F (1,5) = 0.05; r^2 = 0.0009, p = 0.84 [**Fig.4A, top**]; paternal *FMR1* KO: F (1,6) = 1.368; r^2 = 0.19, p = 0.29 [**Fig. 4 A, bottom]**) and 3-chamber (*FMR1* WT: F (1,5) = 0.32; r^2 = 0.06, p = 0.60 [**Fig. 4D, top**]; paternal *FMR1* KO: F (1,6) = 0.24; r^2 = 0.04, p = 0.64 [**Fig. 4D, bottom**]) behavioral performances, indicating that maternal *FMR1* KO allele transmission presents FXS penetrance due to higher mutant cell density within these defined behavioral networks of brain regions. We subsequently determined how well healthy cell density percent within OFT or 3-chamber ROI networks could model and distinguish WT from mutant behavioral performance using data from all mice (n=22) studied (**Fig. 4 B-C, E-F**). Likelihood-ratio tests performed on binary logistic regression models revealed that healthy cell density percent in ROI networks significantly predicts wild-type or mutant performance outcome in both OFT ($x^2(1)$ = 16.245; log-likelihood ratio = -14.4206; p = 0.00006) (**Fig. 4C**) and 3-chamber ($x^2(1)$ = 8.8254; log-likelihood ratio = -12.891; p = 0.003) (**Fig. 4F**) assays. The equal-odds ratio of wild-type/mutant behavioral outcome

was calculated at 55.20 ± 5.95% healthy cell density percent in the OFT ROI network and 49.18 ± 5.19% healthy cell density percent in the 3-chamber ROI network.

DISCUSSION

Random XCI in females is thought to provide a compensatory mechanism to balance X-linked traits and disease at the cellular level. We have quantitatively captured X-linked inheritance patterns in the female brain and by extension, the modes by which they govern a disease state. The average female mouse brain contained 20%, or 8 million more Xm-active cells than Xp, which lacked a preference of anatomical location. Whole-brain XCI status of individuals was globally represented across all regions studied with stochastic region-to-region fluctuations of up to 52%. Collectively, these features mechanistically linked behavioral penetrance of female FXS: maternal inheritance of the mutant allele was required for an underlying 50% mutant cell density threshold to be reached, allowing for FXS presentation in sensorimotor, spatial memory, and sociability behaviors. We confined this effect to structurally connected brain networks, or circuits, underlying arena exploration and sociability.

FXS occurs in human females preferentially upon maternal transmission (*29, 30*), and leads to autism spectrum disorder (ASD) in 20% of cases (*31*). FXS females exhibit anxiety, avoidance (*32*), and hyper-reactivity (*33*) upon social stimuli. We show that maternal *FMR1* KO mice avoid occupancy in the social chamber and the control empty cup chamber. Instead, they spend abnormally more time occupying and traveling within the center chamber. This effect was likely driven by the >50% mutant cell density found within an integrated circuit of ROIs characterizing spatial encoding (e.g. ENTm, VISl) and social (e.g. MPN, BST, DGmo) behavioral functions. Female FXS mice therefore provide a model which phenocopies human FXS social defects, and our data reveals the regional identity of a putative circuit underlying the behavior. Equally, exploratory drive to the center of the OFT sensorimotor assay was defective in maternal *FMR1* KO allele carriers. This defect localized to >50% mutant cell density in a separate circuit of subcortical regions that communicate (e.g. VPL, POL, DCO, CN, SPVO) and integrate (e.g. NDB, MA, VLPO, ZI) sensory and motor (e.g. GPi, GPe) information. Abnormal sensory processing including sensory hypersensitivity is a hallmark feature in human FXS (*34*) and auditory hyper-excitability is used as a robust translatable biomarker of FXS in male *FMR1* KO mice (*35*). Our results therefore suggest involvement of the identified OFT circuit of ROIs in defective sensory processing and integration in human FXS patients. Taken together, the broad and various behavioral effects observed in FXS may manifest through a circuit-autonomous fashion, with each circuit separately relying on the balance of healthy/mutant cell ratios for proper functioning and behavioral output (**Fig. 4B, E**).

In summary, we propose that FXS, and potentially other X-linked syndromes, is conditionally presented in females due to the distributed amount of transcriptionally active mutant cells populating behavioral circuits. XCI chooses X-linked circuit cell amount during development, and presents permissive or restrictive conditions on behavior pending the healthy/mutant cellular ratio reached. Unbalanced brain XCI and region-to-region stochasticity affect these ratios, thereby providing rules of female X-

linked inheritance of behavioral traits and specifically at the level of circuits. Our results and others' underscore a 'cell quantity-based mutational load' theory of FXS behavioral penetrance, whereby the quantity of mutant cells regulate the overall effect on phenotype. Remarkably, a 50/50% balance in healthy/mutant cells may provide a threshold for penetrance: 50-100% healthy cell density in behavioral circuits prevents deficits in female sensorimotor and sociability behavior, and ectopic FMRP redelivery non-specifically in 50% of cells has been shown to rescue male *FMR1* KO repetitive behavior (*36*), as well as motor, anxiety, and sensorimotor defects (*37*). Future work within different behavioral paradigms and in other X-linked disease contexts will hopefully identify more circuits of penetrance and address the translatability of our current findings towards other disease, respectively. An underlying brain network basis of FXS penetrance presents a new avenue for therapy, albeit with the challenge of achieving spatial specificity in treatment. Exacerbation of symptoms can occur if viral treatment causes FMRP levels to rise past physiological levels, highlighting importance in female treatment specificity (*37*). Future therapeutic ventures should therefore be guided by display of behavioral defects specifically presented on a patient by patient basis, and avoid pharmaceuticals that work non-autonomously across behavioral circuits of the brain.

ACKNOWLEDGEMENTS

We would like to thank CSHL Hillside animal husbandry services for their support and efforts. E.S. thanks all members of the Osten lab for inputs on the study. This work was funded by the United States National Institute of Health grants R01 MH096946 and U01 MH105971 to P.O.

AUTHOR CONTRIBUTIONS

E.S. and P.O. conceptualized the study. E.S., P.O., and Y.K. designed all imaging experiments. R.P. performed all genotyping and assisted with animal husbandry and experimental design. E.S. and K.U.V. implemented CN algorithms for automated cell detection. E.S. optimized algorithm detection settings for MeCP2-EGFP+ nuclei detection. E.S. designed and D.F. performed all behavioral experiments. E.S. and D.F. performed ovariectomies. E.S. performed all animal tissue processing and imaging experiments. E.S. performed data analyses for Figs. 1, 2, 3A, and 4A, D. J.K. and J.A.H. designed and performed structural connectivity weight analyses for brain networks. J.A.G. performed logistic regression analyses. E.S. wrote the manuscript.

Szelenyi Fig. 1

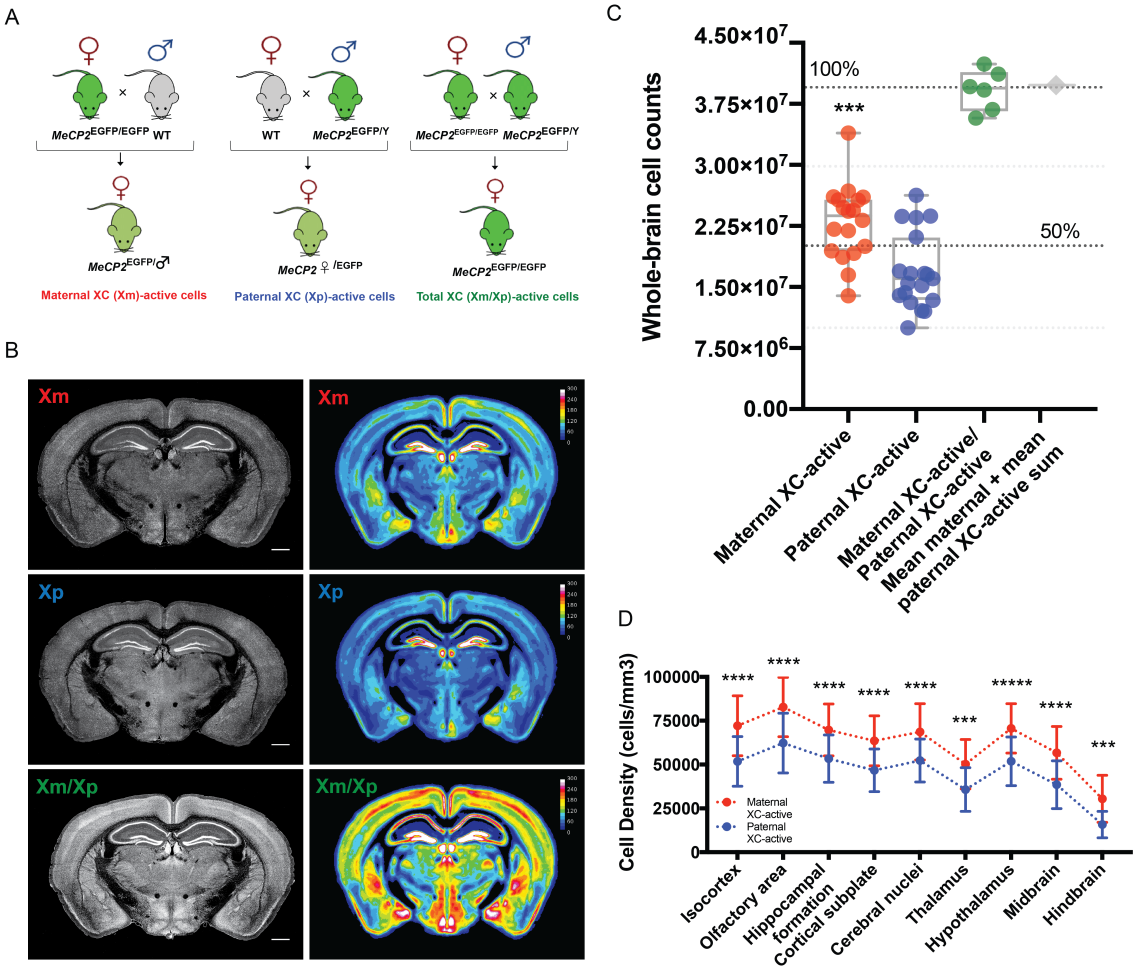

Figure 1: Whole-brain quantification of active X chromosome containing cells with known parent-of-origin. A) Schematic of maternal, paternal, and homozygous XCa cellular reporter derivation. Female mice containing maternal (bottom left) or paternal (bottom middle) XCa-reporting cells were visualized and measured through native MeCP2-EGFP cellular labeling. Whole-brain processing was performed on female offspring from homozygous female ($MeCP2^{EGFP/EGFP}$; left) and wild type male mice crosses to label maternal XC-active cells, or hemizygous male ($MeCP2^{EGFP/Y}$; right) and wild type female crosses to label paternal XC-active cells, respectively. 100% control homozygous reporter mice (bottom right) were obtained by crossing homozygous females ($MeCP2^{EGFP/EGFP}$) with hemizygous males ($MeCP2^{EGFP/Y}$). B) Representative STP-generated coronal images (grayscale; left) of maternal (Xm, top), paternal (Xp, center), and homozygous (Xm/Xp, bottom) MeCP2-EGFP reporter brains (scale bar = 750 um). Mean cell counts of each genotype for corresponding sections in a) are visualized as a heat map in warped voxelized space (right). Heat map color legend of each example is shown to the right on a 16-color gradient scale from white (max; 300 cells/voxel), yellow (middle; 150 cells/voxel), to black (0 cells/voxel). C) Absolute whole-brain cell counts of maternal (red; n=18), paternal (blue; n=19), and homozygous (green; n=6) MeCP2-EGFP reporters. The mean sum of heterozygous groups are plotted on the far right with dashed lines indicating 100% (top) or 50% (middle) total possible counts based on this value. ***$p<0.005$ D) Mean cell density (cells/mm^3) ± SD across major ontological divisions of the brain for Xm-active (red) and Xp-active (blue) reporter mice. ***$q<0.005$; ****$q<0.001$versus paternal XC-active brains.

Szelenyi Fig. 2

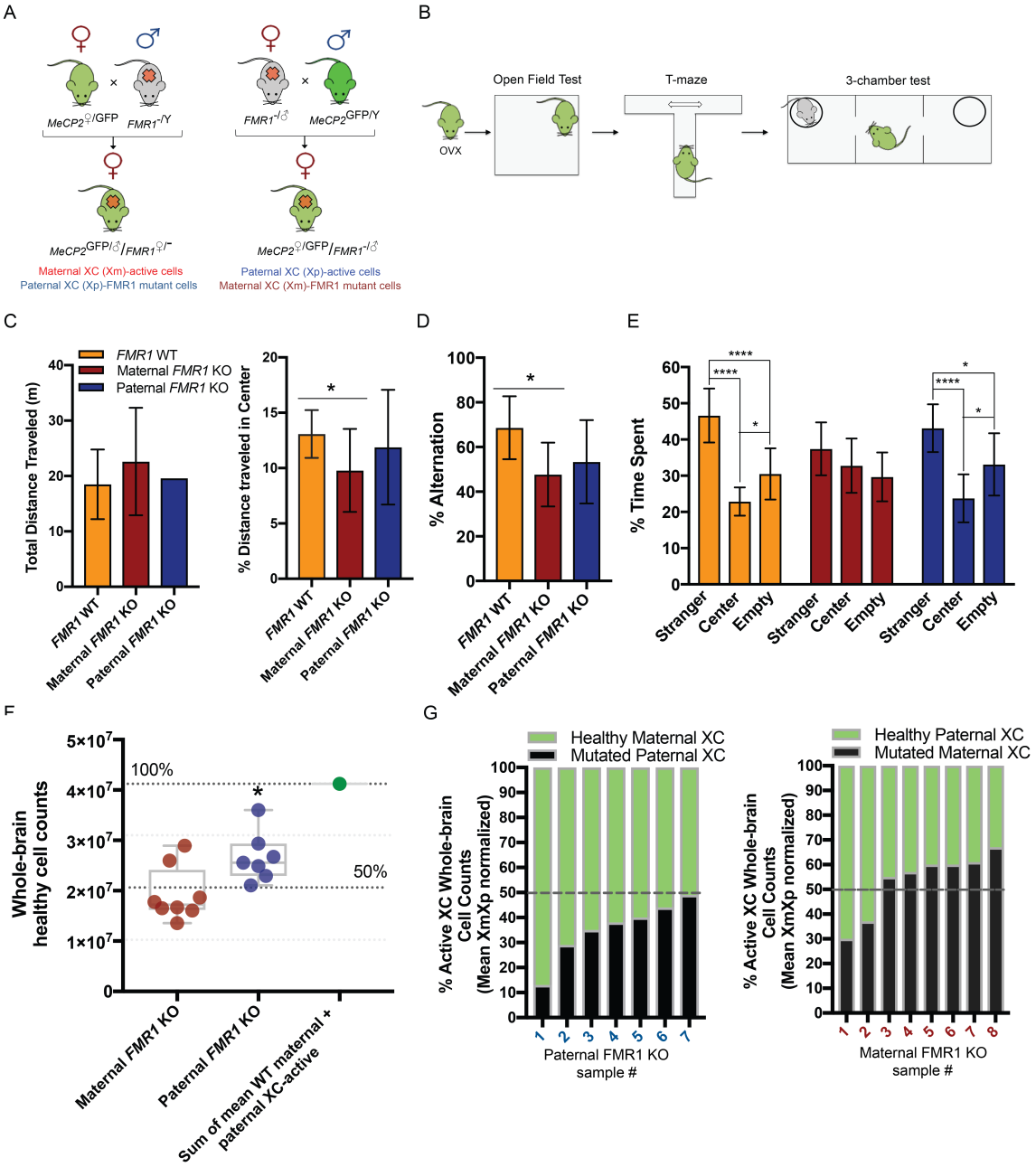

Figure 2: Parent-of-origin effects in a mouse model of female Fragile X syndrome. A) Derivation of maternal XCa-reporting/paternal *FMR1* KO ($Xm^{MeCP2\text{-}EGFP}/Xp^{FMR1\ KO}$) and paternal XCa-reporting/maternal *FMR1* KO ($Xp^{MeCP2\text{-}EGFP}/Xm^{FMR1\ KO}$) double heterozygous female mice used for behavioral assays and whole-brain imaging. B) Sequence of behavioral testing performed. All mice were ovariectomized at least 2 weeks prior to open field test, T-maze, and 3-chamber test of sociability. Behavioral data used for analyses were from the same mice across assays. A subset of these mice was used for whole-brain imaging experiments. All tests were separated by 2-7 days. C-E) Behavioral assay results. C) Total distance traveled (left) and percent distance traveled in center of the arena (right) compared amongst *FMR1* WT (n=8; left), maternal *FMR1* KO (n=9; middle), and paternal *FMR1* KO (n=8; right) genotype from the OFT. D) Percent alternation performance from the T-maze test of spatial memory. E) Percent time spent in stranger, center, or empty chamber during a 3-chamber test of sociability. *$q<0.05$; **$q<0.01$; ***$q<0.005$; ****$q<0.001$ F) Whole-brain XCI in *FMR1* mutant mice. Whole-brain healthy cell counts of maternal *FMR1* KO ($Xm^{FMR1\ KO}/Xp^{MeCP2\text{-}EGFP}$; n=8) and paternal *FMR1* KO ($Xm^{MeCP2\text{-}EGFP}/Xp^{FMR1}$ KO; n=8) mice. *$p<0.05$. 100% control reference, the sum of mean *FMR1* WT whole-brain cell counts are shown to the right with dashed lines indicating 100% (top) or 50% (middle) total possible cell counts based on this value. G) Stacked 100% bar graphs of individual whole-brain XCa cell counts from F), normalized to mean $Xm^{MeCP2\text{-}EGFP}/Xp^{MeCP2\text{-}EGFP}$ values for maternal (left) and paternal (right) *FMR1* KO mice. Percent XCa for each brain is shown as measured healthy active-XC (green) and estimated mutant active-XC (black).

Szelenyi Fig. 3

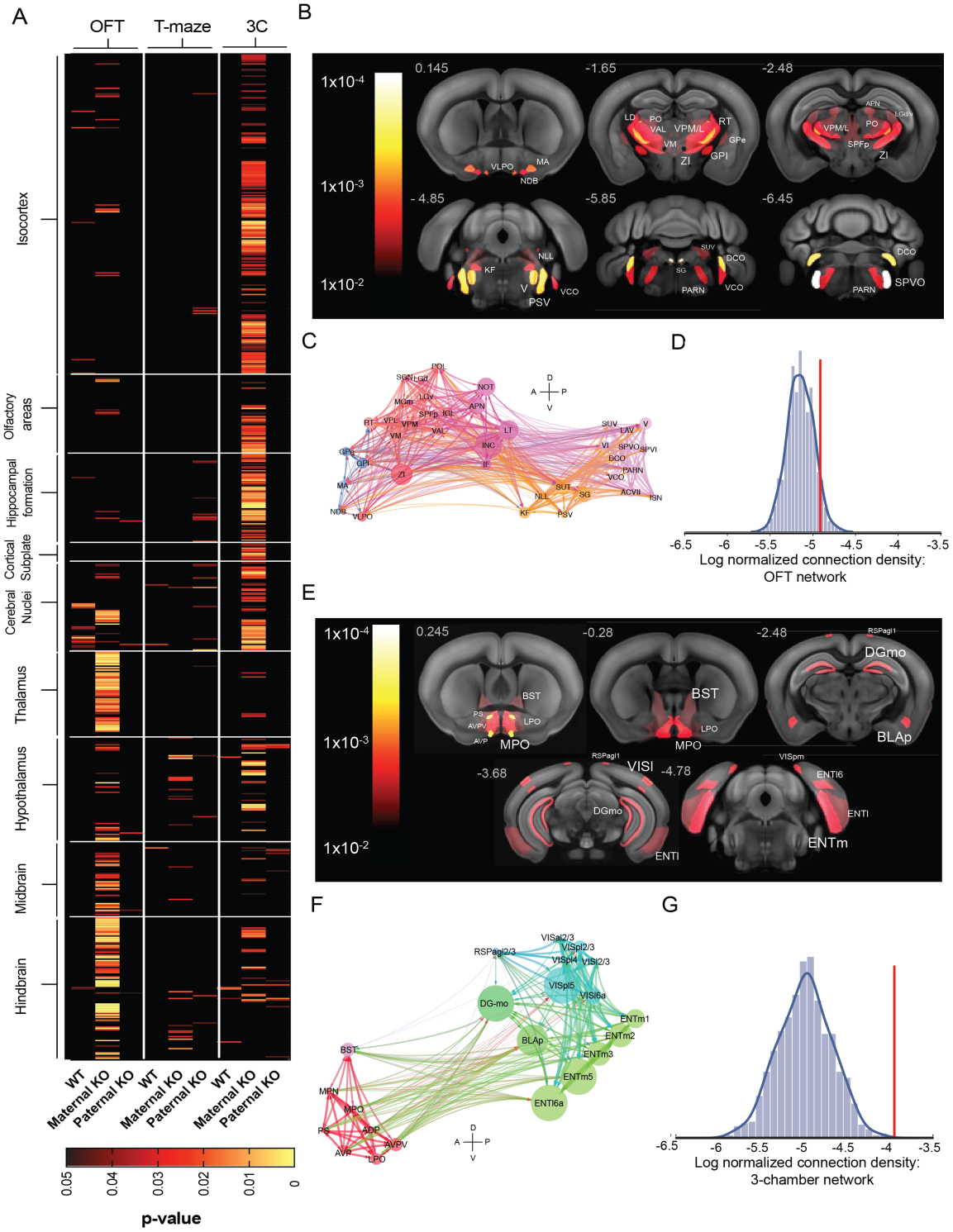

Figure 3: Localization of FXS behavioral penetrance using ROI-based correlational screens. A) Pearson's correlational analysis conducted amongst behavioral scores and brain-wide healthy ROI cell density. Data is displayed in a 2-dimensional (ROI - y-axis; genotype/behavioral test – x-axis) heat map of significant p-values represented on a double color gradient from 0.05 (black), 0.025 (red), to 0 (yellow). Scale legend is listed at the bottom. Results from *FMR1* WT, maternal and paternal *FMR1* KO mice (x-axis) are grouped by each behavioral test (left - OFT, center – T-maze, right - 3-chamber) and ROIs are listed in order of major hierarchical brain structures. B) Significant ROIs (p=0.01 threshold) from maternal *FMR1* KO OFT screening results found in A), heat mapped and overlaid in reference brain space. Individual names of significant ROIs and anterior/posterior location with respect to bregma are listed for each section shown. C) Visualization of structural connectivity weights within the significantly correlated OFT ROI network (**Methods**). ROI node and edge color assignment is based on major brain structure colors as defined by Allen Brain Atlas (http://atlas.brain-map.org). D) Normalized median connection density of OFT ROI network (red line), and 1000 in-silico generated random ROI networks of the same inter-regional distance and ROI amount (gray). Data is compared and presented on a log10 scale. E-G) 3-chamber ROI network data presented and compared the same as panels B-D). ROI acronyms: B, C) VLPO – ventrolateral preoptic area; NDB – nucleus of the diagonal band; MA – magnocellular nucleus; PO – posterior complex of the thalamus; VPM/L – ventral posteromedial/lateral nucleus of the thalamus; PC – paracentral nucleus; RT – reticular nucleus of the thalamus; ZI – zona incerta; GPi – globus pallidus, internal; GPe – globus pallidus, external; SPFp – subparafacsicular nucleus, parvicellular part; LGv – ventral part of the lateral geniculate nucleus; LGd – dorsal part of the lateral geniculate nucleus; KF – Koelliker-Fuse subnucleus; V – motor nucleus of the trigeminal; PSV – principal sensory nucleus of the trigeminal; VCO – ventral cochlear nucleus; SG – supragenual nucleus; DCO – dorsal cochlear nucleus; VCO – ventral cochlear nucleus; SPVO – spinal nucleus of the trigeminal, oral part, E, F) PS – parastrial nucleus; BST – bed nuclei of the stria terminalis; AVP – anteroventral peoptic nucleus; AVPV – anteroventral periventricular nucleus; MPO – medial preoptic nucleus; LPO – lateral preoptic area; RSPAgl – retrosplenial cortex, agranular layer; DGmo – dentate gyrus, molecular layer; BLAp – basolateral amygdala, posterior; VISpm – posteromedial visual area; VISl - lateral visual area; ENTl – entorhinal area, lateral; ENTm – entorhinal area, medial

Szelenyi Fig. 4

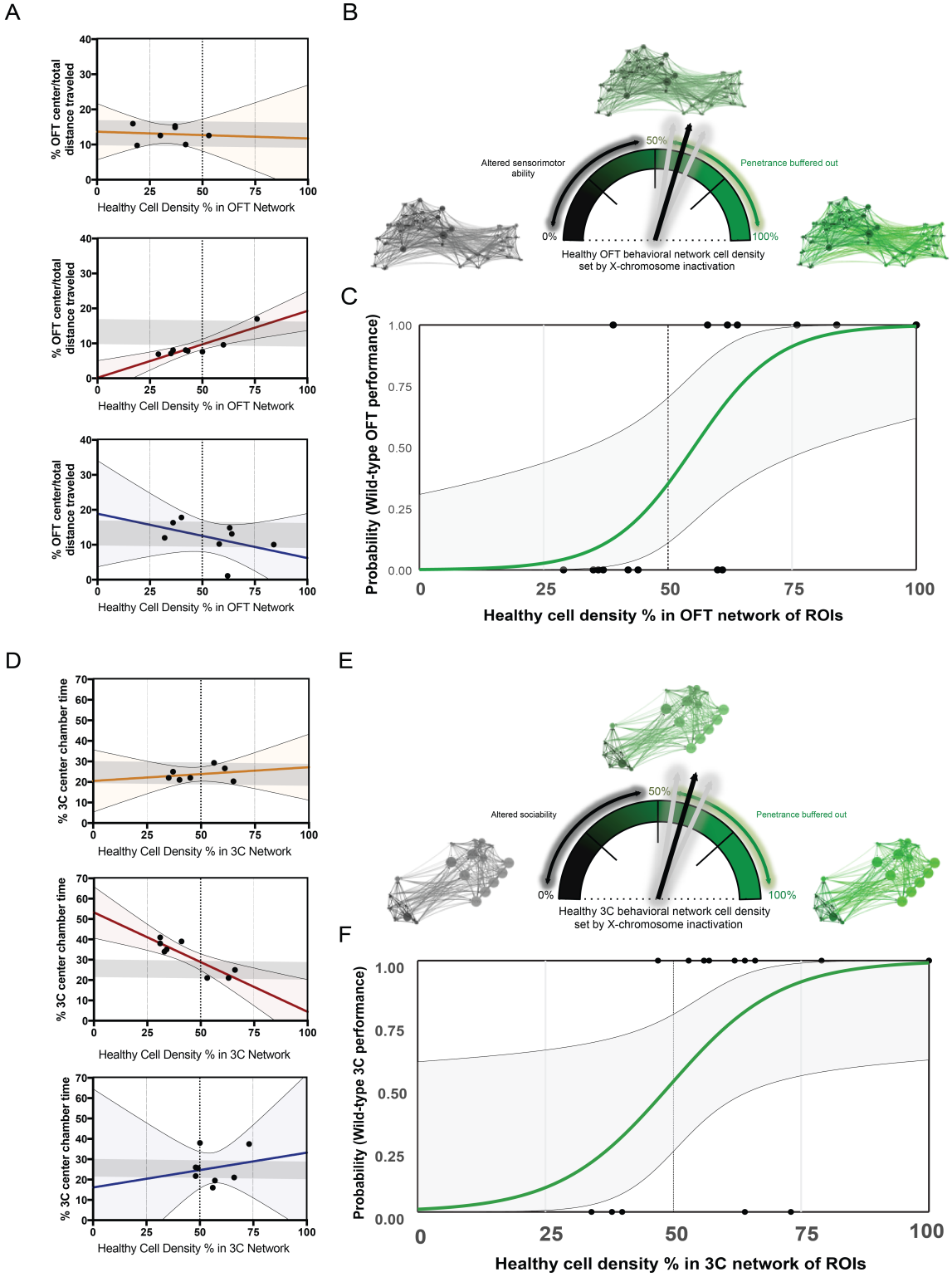

Figure 4: Dependence of female FXS outcome on healthy cell density in brain networks. A-C) OFT network regression analyses. A) Linear regression of percent distance traveled in center of OFT due to healthy cell density percent in OFT network for *FMR1* WT (top), maternal *FMR1* KO (center), and paternal *FMR1* KO female mice (bottom). Shadowed rectangle in each group represents control *FMR1* WT range of behavioral scores for comparison. B) Schematic depiction of OFT network analyses from A), in which percent of healthy cell density in the OFT network determines if mice display altered sensorimotor ability or if the penetrance is buffered out due to lack of mutant cell amount needed for an effect. C) Logistic regression modeling of WT OFT behavioral performance probability due to percent of healthy cell density in OFT network. Grayed area represents ± 95% confidence intervals. D-F) 3-chamber (3C) network regression analyses. D) Linear regression of percent time spent in center chamber of 3-chamber due to healthy cell density percent in 3C network for *FMR1* WT (top), maternal *FMR1* KO (center), and paternal *FMR1* KO female mice (bottom). E) Schematic depiction of 3C network analyses from A), in which percent of healthy cell density in the 3C network determines if mice display altered sociability or if the penetrance is buffered out. C) Logistic regression modeling of wild-type 3C behavioral performance probability due to percent of healthy cell density in 3C network. Grayed area represents 95% confidence intervals.

MATERIALS AND METHODS

Animal breeding and husbandry. Adult mice (8-10 weeks old) were used for whole-brain imaging experiments. Animals were housed under a 12-hour light/dark cycle (0600 ON, 1800 OFF), had access to food and water ad libitum, and were housed with littermates. All experimental procedures were performed in accordance with CSHL Animal Care and Use Committee Guidelines. The MeCP2-GFP mouse line was obtained from the Jackson laboratory (stock # 014610). MeCP2 is a gene located at chromosomal position X A7.3 and is subject to XCI. Developed in the laboratory of Adrian Bird, this mouse line contains an in-frame EGFP knock-in cassette at the 3' UTR of the MeCP2 locus ((*14-17*). Driven and regulated by the endogenous MeCP2 promoter/enhancers, MeCP2-EGFP expression leads to normal MeCP2 levels and subcellular localization of MeCP2 protein that is fused at the C-terminus with EGFP. Expression of the fusion allele does not alter neuronal physiology (*16*) and mice are successfully bred to homozygosity without behavioral or reproductive complications (data not shown). In addition, strong expression of MeCP2-EGFP favors neurons of many types (*15*) thereby circumventing biased effects of XCI determinations based on expression profile. Maternal ($Xm^{MeCP2\text{-}EGFP}/Xp^{MeCP2\ WT}$) or paternal ($Xm^{MeCP2\ WT}/Xp^{MeCP2\text{-}EGFP}$) XCa cellular reporter mice were obtained in separate heterozygotes by crossing homozygous females (*MeCP2*$^{EGFP/EGFP}$) or hemizygous males (*MeCP2*$^{EGFP/Y}$), respectively, with wild-type C57Bl6/J (JAX stock # 000664) mice. A subset of these wild-type reporter mice were derived from *FMR1* KO or WT crosses that generated $Xm^{FMR1\ WT}/Xp^{MeCP2\text{-}EGFP}$ and $Xm^{MeCP2\text{-}EGFP}/Xp^{FMR1\ WT}$ reporter brains (below) that are congenic to the C57Bl6/J crosses. Homozygous reporter mice were obtained by crossing *MeCP2*$^{EGFP/EGFP}$ females with *MeCP2*$^{EGFP/Y}$ males. *FMR1* KO mice were obtained from the Jackson laboratory (#003025). These mice were originally developed in the Oostra laboratory and contain a gene-disrupting neomycin resistance cassette in exon 5 of the FMR1 locus (*21*). Maternal XCa-reporting, paternal *FMR1* KO ($Xm^{MeCP2\text{-}EGFP}/Xp^{FMR1\ KO}$) female mice were generated by breeding homozygous *MeCP2*$^{GFP/GFP}$ females with hemizygous *FMR1*$^{KO/Y}$ males. For imaging only, $Xm^{MeCP2\text{-}EGFP}/Xp^{FMR1\ WT}$ female mice were generated by separately breeding homozygous *MeCP2*$^{EGFP/EGFP}$ females with hemizygous *FMR1*$^{WT/Y}$ males. Conversely, paternal XCa-reporting, maternal *FMR1* KO ($Xm^{FMR1\ KO}/Xp^{MeCP2\text{-}EGFP}$) or WT littermate ($Xm^{FMR1\ WT}/Xp^{MeCP2\text{-}EGFP}$) female mice were generated by breeding heterozygous *FMR1* KO females with hemizygous *MeCP2*$^{GFP/Y}$ males. Using this strategy, maternal *FMR1* KO mice have healthy paternal XCa expression tracked with the MeCP2-EGFP allele while the reciprocal cross produces paternal *FMR1* KOs with XCa cellular tracking through the maternal MeCP2-EGFP allele. All transgenic mice were maintained on a C57Bl6/J background.

Brain sample preparation. Animals were euthanized via transcardial perfusion under ketamine/dexmedetomidine anesthesia. Dissected brains were post-fixed overnight in 4% paraformaldehyde at 4 C, incubated for 48 h in 0.1 M glycine/0.1 M PB for auto fluorescent quenching, and then stored in 0.05 M PB at 4 C until confocal or serial two-photon tomography imaging (STPT; see below). Prior to STPT imaging, brains were embedded 4% oxidized agarose in 0.05 M PB using custom molds and holders to maintain consistent embedding position. Embedded brains were crosslinked in 0.2%

sodium borohydrate solution for 3h at room temperature or overnight at 4 C prior to STPT processing (below).

Immunohistochemistry and confocal imaging. Neuronal expression of the MeCP2-EGFP allele was studied though immunostaining and confocal imaging. 50 um vibratome-processed, free-floating coronal sections of homozygous *MeCP2*$^{GFP/GFP}$ reporter mice brains (n=2) were processed. Sections were washed 3 times in PBS followed by blocking for 1 h at room temperature in PBS- T (PBS, 0.2% Triton-X 100) containing 5% donkey serum. Sections were then incubated overnight at 4 C in blocking solution containing rabbit anti-NeuN (Millipore, ABN78) primary antibody at 1:1000. After washing, NeuN-stained sections were incubated with anti-rabbit AlexaFluor-568-conjugated secondary antibody (Thermo-Scientific, A10042) diluted 1:500 for 1 h at room temperature. After washing excess secondary antibody, sections were mounted, DAPI- counterstained (Prolong Gold Antifade Mountant, Thermo Fisher), and coverslipped for imaging. Confocal images were acquired with a Zeiss LSM780 confocal microscope using a 561 laser and corresponding dichroic and filter sets. Single plane images were captured with a 40x oil immersion objective. Total colocalized populations for each marker of every FOV (212.55 um X x 212.55 um Y) were manually quantified using Fiji image processing package.

STPT imaging. The Tissuecyte1000 instrument was used for all imaging experiments (Tissuevision) (*12*). This system combines a high-speed multi- photon microscope with a fully integrated vibratome for automated z-sectioning and image acquisition throughout the entire whole-mount sample. Embedded sample brains were imaged with a 20x objective at 50 uM below the sample surface. 270 total serial sections were acquired at 50 um z-resolution (13.5 mm total z-length), with each section being comprised of a 12 (x-axis, 700 um) x 16 (y-axis, 700 um) field of view (FOV) mosaic. Images were acquired with laser scan settings of 1 um/pixel at an integration time of 1 us. A laser wavelength of 910 nm with ~322 mW power at the end of the objective was used for optimal excitation/emission of MeCP2-EGFP fluorescence. Constant laser settings and PMT detector settings were used for all samples.

Automated MeCP2-EGFP+ cellular detection and counting. Raw image tiles for each brain were illumination corrected, stitched in 2D with Matlab and aligned in 3D using Fiji software (*12*). For reliable automated MeCP2-EGFP detection from full brain datasets, we implemented convolutional networks (CNs) (*38*). CN training for detection of MeCP2-EGFP+ cells in the STPT datasets was accomplished as in previous studies (*13*) with CN training performed on human marked-up ground truth data (biological expert identified MeCP2-EGFP+ nuclei) of MeCP2-EGFP brains. CN performance was determined based on F-score calculations (F-score = the harmonic mean of the precision and recall, where precision is the ratio of correctly predicted cells divided by all predicted cells and recall is ratio of correctly predicted cells divided by ground truth positive cells; ~1800 MeCP2-EGFP+ cells were marked/expert/brain). Composite F-scores for MeCP2-EGFP CN was obtained by determining F-scores in 8 FOVs (400 (X) um by 400 (Y) um) representing different cellular density and imaging content in 3 separate heterozygous

MeCP2-EGFP+ brains (24 FOVs total). Stable precision and recall was seen for all regions analyzed, delivering a composite F-score of 0.84 (**Fig.1S2C-E**). In the CN output images, signal smaller than 10 μm^2 was removed as noise. In order to normalize the performance of CN for each brain, the brightness of MeCP2-EGFP+ signal for each sample was normalized by the mean and standard deviation of tissue autofluorescence signal from a coronal section corresponding to bregma position of +0.20 mm. We did not analyze MeCP2-EGFP+ cells in the cerebellum due to faulty brain-to-brain warping of this region (data not shown).

3D brain registration and anatomical segmentation. Registration of individual brains to a standardized reference space was computationally achieved as published previously (*13*). In short, affine transform was calculated using 4 resolution levels and B-spline with 3. Advanced Mattes mutual information (*39*) was the metric used to measure similarity between moving and fixed images. Image similarity function is estimated and minimized for a set of randomly chosen samples with each 23 images in a multi-resolution and iterative fashion (*12*). Entire warping of whole-brain images is done using elastix (*40*). Anatomical segmentation of Allen Brain Atlas (ABA) labels onto sample brains was made possible also as previously published (*13*). Version 2.2 ABA labels (836 total) were transformed onto individually registered samples. Quality control of ROI segmentation found and excluded 95 ROIs total from analysis due to erroneous counting most likely caused by small ROI size and/or warping location (**Supplementary Table 1**). In addition, cell counts from layer 6 a and b were combined into one layer, layer a.

2D-3D cell count correction and density measurements. Detected 2D cell count values obtained at 50 um Z resolution were transformed by a stereological 3D conversion factor obtained by the following way (**Fig. 1S2A, B**). First, counting boxes of 200 um x 200 um x 50 um (xyz) were acquired at 2.5 um Z resolution via optical imaging within 6 brain regions comprising major anatomical divisions of a female heterozygous MeCP2-GFP mouse brain. 20 optical images were acquired at a depth range that spanned 50 um around the normal 50 um focal depth (i.e. 25-75 um below the tissue surface). Second, MeCP2-EGFP CN was run on the middle optical section corresponding to the 50 um depth. Third, manual markup of MeCP2-EGFP+ nuclei was performed in each counting box using the stereological counting rules of Williams and Rakic (*41*). Lastly, a conversion factor for each region was calculated by dividing manual 3D counts by 2D CN count of the middle section. This factor was averaged over the 6 regions reaching a final conversion factor of 2.6. (**Fig. 1S2B**). ROI cellular density was obtained by 1) transforming ABA labels onto individual brains, 2) converting ROI assigned pixel space to mm^3, 3) dividing 2.5 um Z-corrected absolute cell counts by mm^3 values by to arrive at cells/mm3.

Behavioral testing. 6-8 month old ovariectomized female mice were behaviorally phenotyped in a sequential series of tests. All mice were ovariectomized at least 2 weeks prior to testing in order to remove estrous cycle influences from behavior. Each behavioral test was separated by 2-7 days to avoid acute post-testing and handling effects. $Xm^{FMR1\ WT}/Xp^{MeCP2\text{-}GFP}$ mice served as behavioral controls for all behaviors studied. The following tests were sequentially performed on each mouse:

Open field test (OFT). To measure activity and anxiety in an open field, unhabituated mice were placed in a 40 x 40 x 40 cm2 open plexiglass box containing a layer of fresh bedding. The open field arena was located in a non-sound-proof, enclosed environment under dim lighting. All mice were housed in the same facility room behavioral testing was performed. An overhead camera visually captured all tests and ANY-maze (Stoelting) automated behavior tracking software was used for real-time activity/location recording and analysis. A 20 x 20 cm center square designated within the tracking settings defined the center and perimeter boundaries of the arena. The software measured total and center distance traveled. For center-specific activity, center distance was normalized to total distance traveled and presented as percent total distance traveled. Adequate cleaning of the maze with bleach, water and drying was performed between each mouse. Fresh bedding was added to the arena for each subject.

T-maze. We studied mouse spatial memory by measuring spontaneous spatial alternations in the T-maze (*42, 43*). Spontaneous alternation is an innate exploratory behavior possessed by rodents which is hippocampus-dependent and serves as an index of spatial and working memory (*42*). Our protocol was based off of the continuous version with minor modification (*43*). The dimensions of the T-maze used was 35 cm stem length, 28 cm arm length, 10 cm arm height, and 5 cm lane width (Stoelting). For testing, the T-maze was located in a non-sound-proof, enclosed environment under dim lighting. All mice were housed in the same facility room behavioral testing was performed in. To begin the test, each mouse was carefully placed at the stem start position of the maze and was freely allowed to enter either arm. To prevent the mouse from entering the other arm after its initial choice, a metal block was placed at the entrance of the empty arm once the subject committed exploration to an arm. The subjects were allowed to freely explore the chosen arm and stem until it explored back to start of the stem. Once the beginning position was reached, the mouse was held in-between the start position and a metal block placed proximally to the start position for 5 seconds. The metal block was then removed and the mouse was allowed again to enter an arm of its choice. Manual scoring of each arm choice and time to experimental completion was made after 14 trials. No more than 3 minutes/trial was allowed for each subject and encouragement was given to each subject at 3 minutes (in the form of hand movement behind the mouse) to return to start position. Mice that did not complete more than 9 trials were excluded from analysis. Adequate cleaning of the maze with bleach, water and drying was performed between each mouse. The number of trial-to-trial arm entry alternations (e.g. left-to-right or right-to-left) was calculated and expressed as a percent of total trials.

3-chamber test. Sociability was measured using the 3-chamber test. The 3-chamber apparatus used consisted of a plexiglass box (60 x 40 x 22(h) cm) partitioned into 3 chambers (20 cm/each) (Stoelting). Doors (4 x 8 cm) connecting chambers allowed the mice to freely explore all areas of the box. The apparatus was located in a non-sound-proof, enclosed environment under dim lighting. All mice were housed in the same facility room that behavioral testing was performed in. An overhead camera visually captured all test sessions and ANY-maze (Stoelting) automated behavior tracking software was used for real-time activity/location recording and analysis. Chamber

designations in tracking software were user-defined and used for chamber-specific activity measurements. Two metal-barred cylindrical cages (7 cm (diameter) x 15 cm (height); 3 mm bar diameter and 7 mm spacing) were used for stranger mouse containment in one chamber and for an empty enclosure in the opposite-sided chamber. The cage bars are spaced such that close sniffing is the only interaction type possible. Ovariectomized adult female *FMR1* WT mice were used as stranger mice and were habituated to an enclosure cage for 10 minutes at least 1 day prior to any experiments. Each stranger mouse (n=8) was used 4 times only and were rotated every 4 experiments for use. Test mice were habituated to an empty 3 chamber apparatus for 10 minutes prior to actual experiments. For testing, mice were allowed to freely explore all chambers for 10 minutes. For each experiment the enclosed stranger mouse was placed in the left chamber and the empty enclosure on the right. Chamber time spent and distance traveled was quantified for each chamber. Percent time spent or distance traveled was calculated as total value/individual chamber value.

Quantification of structural connectivity within correlated brain networks of ROIs. We determined if OFT and 3-chamber correlated ROIs groups (i.e. all ROIs reaching $p \leq 0.01$ correlation; herein referred to as "networks") represented structural connectivity networks by comparing the median ROI network connection weight to a distribution of randomly sampled networks of the same size for both tasks. We use the normalized connection density, a measure of connection strength normalized by both source and target region sizes, from the regional structural connectivity matrix (*44*). We restricted the population of structures for each network to ROIs from which we could draw to an intermediate level of the ontology represented by 292 'summary structures' (*28*). The intersection of these summary structures with the sets of ROIs for each task resulted in sets of 39 and 13 ROIs for the open field and 3-chamber tasks, respectively. Additionally, since mesoscale connectivity is distance dependent (*28*) and the model in Knox et al is spatially dependent (*44*), we restricted the selection of random ROI networks to have similar inter-regional distance dependence as that of their respective cell density correlated ROI networks.

The procedure for this selection is as follows:

Given a set of N cell density correlated summary structure level ROIs:
1) Randomly draw a set of N regions from the set of summary structures.
2) Compute the pairwise inter-regional distances for the set of sampled regions.
3) Compute the Kolmogorov-Smirnov statistic to measure the difference in distributions of distances for the sampled and cell-count correlated networks
a) If the KS statistic shows a significant difference in distributions (having a p-value < 0.01), reject the sample and return to (1).
b) Else, return the sample

The above procedure is repeated 1000 times, after which the median normalized connection density of the experimental ROI networks is compared to the distribution of random sample medians. Since these connectivity measures are log-normally distributed (*28, 44*), the t statistic is computed in log-transformed space to test the significance of the

difference. Visualization of ROI-ROI connectivity for each ROI network was created with Cytoscape network visualization and analytical program. Significantly correlated ROIs of the deepest ontological distance from root structures were chosen for visualization, except for the ROIs not annotated at the summary structure level and hence not found in the structural connectivity matrix. Those ROIs included: BSTmg, BSTpr, BSTif, BSTpr, PVHap, TTv3, isl, islm, MPNc, MPNl, PAA3, and COApl3. Log-transformed normalized connection densities were used for edge sizes. Edges with sizes < 0 were excluded from the visualization. Between centrality values, a measure of a given node's intermediate relationship to all other nodes of a network, were calculated within Cytoscape and used as node/ROI size. Both edge and node sizes were scaled for figure presentation purposes accordingly. ROIs chosen for visualization represent those reaching $p<0.01$ from the correlational screens, and

Statistics. Whole-brain absolute cell counts were compared amongst Xm-active and Xp-active reporter brains using an unpaired Mann-Whitney U non-parametric t-test. A two-way (2 [Xp or Xm] x 9 [major brain structure]) ANOVA was applied to compare parent-of-origin of reporter allele amongst cell densities of major brain structures. The False Discovery Rate (FDR) method of Benjamini, Krieger, and Yekutieli was used for correcting multiple comparison post-hoc tests of individual comparisons at every structure. Comparisons of genotype amongst OFT and T-maze scores were compared using unpaired Mann-Whitney U t-tests. FDR-corrected post-hoc test comparisons were made against *FMR1* WT and maternal or paternal *FMR1* KO mice scores. Percent chamber time spent and percent distance traveled were compared amongst genotypes and chamber using 3 x 3 factor two-way ANOVAs. Significant within-group differences amongst chambers and between-group differences amongst genotypes were tested with FDR-corrected post-hoc tests. Correlational screens of the association between cell density and behavioral score across 741 ROIs was performed with Pearson's correlation. In this analysis, we did not correct the p-values against Type I error risk, in favor of revealing ROI networks that share behavioral dependencies/relationships. Common correction algorithms such as FDR correct at the family-wise error level and therefore could mask such interdependencies thereby reducing the power and overall intent of the screen. Instead, ROIs with p values less than 0.01 only were visualized in reference brain space and used for downstream analyses. Logistic regression was performed on ROI network healthy cell density percent as the continuous, independent variable and WT performance as the categorical, dependent variable. Mice (n=22) from all genotypes were categorized as WT or mutant performers for each test based on the performance range of *FMR1* WT mice. A likelihood ratio test was performed on each logistic model to determine statistical significance. All statistical testing was performed with Graphpad Prism software version 7.0 and R (R Core Team). Alpha level was set at 0.05 in all analyses except for ROI network modeling whereby all ROIs included for analysis obtained correlational p-values < 0.01.

REFERENCES

1. L. K. Abramowitz, M. S. Bartolomei, Genomic imprinting: recognition and marking of imprinted loci. *Curr Opin Genet Dev* **22**, 72-78 (2012).
2. S. S. Tan, E. A. Williams, P. P. Tam, X-chromosome inactivation occurs at different times in different tissues of the post-implantation mouse embryo. *Nat Genet* **3**, 170-174 (1993).
3. D. K. Nguyen, C. M. Disteche, High expression of the mammalian X chromosome in brain. *Brain Res* **1126**, 46-49 (2006).
4. F. L. Raymond, X linked mental retardation: a clinical guide. *J Med Genet* **43**, 193-200 (2006).
5. E. J. Marco, D. H. Skuse, Autism-lessons from the X chromosome. *Soc Cogn Affect Neurosci* **1**, 183-193 (2006).
6. D. H. Skuse, X-linked genes and mental functioning. *Hum Mol Genet* **14 Spec No 1**, R27-32 (2005).
7. H. Wu *et al*., Cellular resolution maps of X chromosome inactivation: implications for neural development, function, and disease. *Neuron* **81**, 103-119 (2014).
8. J. T. Lee, M. S. Bartolomei, X-inactivation, imprinting, and long noncoding RNAs in health and disease. *Cell* **152**, 1308-1323 (2013).
9. C. Gregg, J. Zhang, J. E. Butler, D. Haig, C. Dulac, Sex-specific parent-of-origin allelic expression in the mouse brain. *Science* **329**, 682-685 (2010).
10. X. Wang, P. D. Soloway, A. G. Clark, Paternally biased X inactivation in mouse neonatal brain. *Genome Biol* **11**, R79 (2010).
11. A. McMahon, M. Fosten, M. Monk, X-chromosome inactivation mosaicism in the three germ layers and the germ line of the mouse embryo. *J Embryol Exp Morphol* **74**, 207-220 (1983).
12. T. Ragan *et al*., Serial two-photon tomography for automated ex vivo mouse brain imaging. *Nat Methods* **9**, 255-258 (2012).
13. Y. Kim *et al*., Mapping social behavior-induced brain activation at cellular resolution in the mouse. *Cell Rep* **10**, 292-305 (2015).
14. K. Brown *et al*., The molecular basis of variable phenotypic severity among common missense mutations causing Rett syndrome. *Hum Mol Genet* **25**, 558-570 (2016).
15. M. J. Lyst *et al*., Rett syndrome mutations abolish the interaction of MeCP2 with the NCoR/SMRT co-repressor. *Nat Neurosci* **16**, 898-902 (2013).
16. F. McLeod *et al*., Reduced seizure threshold and altered network oscillatory properties in a mouse model of Rett syndrome. *Neuroscience* **231**, 195-205 (2013).
17. M. W. Linhoff, S. K. Garg, G. Mandel, A high-resolution imaging approach to investigate chromatin architecture in complex tissues. *Cell* **163**, 246-255 (2015).
18. S. Herculano-Houzel, K. Catania, P. R. Manger, J. H. Kaas, Mammalian Brains Are Made of These: A Dataset of the Numbers and Densities of Neuronal and Nonneuronal Cells in the Brain of Glires, Primates, Scandentia, Eulipotyphlans, Afrotherians and Artiodactyls, and Their Relationship with Body Mass. *Brain Behav Evol* **86**, 145-163 (2015).

19. C. Song *et al*., DNA methylation reader MECP2: cell type- and differentiation stage-specific protein distribution. *Epigenetics Chromatin* **7**, 17 (2014).
20. S. Herculano-Houzel, Coordinated scaling of cortical and cerebellar numbers of neurons. *Front Neuroanat* **4**, 12 (2010).
21. C. E. Bakker *et al*., Fmr1 knockout mice: a model to study fragile X mental retardation. The Dutch-Belgian Fragile X Consortium. *Cell* **78**, 23-33 (1994).
22. B. Vermaercke, G. Van den Bergh, F. Gerich, H. Op de Beeck, Neural discriminability in rat lateral extrastriate cortex and deep but not superficial primary visual cortex correlates with shape discriminability. *Front Neural Circuits* **9**, 24 (2015).
23. M. Fyhn, S. Molden, M. P. Witter, E. I. Moser, M. B. Moser, Spatial representation in the entorhinal cortex. *Science* **305**, 1258-1264 (2004).
24. E. C. Dumont, What is the bed nucleus of the stria terminalis? *Prog Neuropsychopharmacol Biol Psychiatry* **33**, 1289-1290 (2009).
25. D. V. Wang *et al*., Neurons in the amygdala with response-selectivity for anxiety in two ethologically based tests. *PLoS One* **6**, e18739 (2011).
26. J. A. McHenry *et al*., Hormonal gain control of a medial preoptic area social reward circuit. *Nat Neurosci* **20**, 449-458 (2017).
27. C. Leung *et al*., Activation of Entorhinal Cortical Projections to the Dentate Gyrus Underlies Social Memory Retrieval. *Cell Rep* **23**, 2379-2391 (2018).
28. S. W. Oh *et al*., A mesoscale connectome of the mouse brain. *Nature* **508**, 207-214 (2014).
29. D. Z. Loesch, D. A. Hay, Clinical features and reproductive patterns in fragile X female heterozygotes. *J Med Genet* **25**, 407-414 (1988).
30. S. Zeesman *et al*., Paternal transmission of fragile X syndrome. *Am J Med Genet A* **129A**, 184-189 (2004).
31. S. Clifford *et al*., Autism spectrum phenotype in males and females with fragile X full mutation and premutation. *J Autism Dev Disord* **37**, 738-747 (2007).
32. T. A. Williams, M. A. Porter, R. Langdon, Social approach and emotion recognition in fragile X syndrome. *Am J Intellect Dev Disabil* **119**, 133-150 (2014).
33. T. A. Williams, R. Langdon, M. A. Porter, Hyper-reactivity in fragile X syndrome females: generalised or specific to socially-salient stimuli? A skin conductance study. *Int J Psychophysiol* **88**, 26-34 (2013).
34. M. Rais, D. K. Binder, K. A. Razak, I. M. Ethell, Sensory Processing Phenotypes in Fragile X Syndrome. *ASN Neuro* **10**, 1759091418801092 (2018).
35. S. Rotschafer, K. Razak, Altered auditory processing in a mouse model of fragile X syndrome. *Brain Res* **1506**, 12-24 (2013).
36. S. Gholizadeh, J. Arsenault, I. C. Xuan, L. K. Pacey, D. R. Hampson, Reduced phenotypic severity following adeno-associated virus-mediated Fmr1 gene delivery in fragile X mice. *Neuropsychopharmacology* **39**, 3100-3111 (2014).
37. J. Arsenault *et al*., FMRP Expression Levels in Mouse Central Nervous System Neurons Determine Behavioral Phenotype. *Hum Gene Ther* **27**, 982-996 (2016).
38. S. C. Turaga *et al*., Convolutional networks can learn to generate affinity graphs for image segmentation. *Neural Comput* **22**, 511-538 (2010).

39. D. Mattes, D. R. Haynor, H. Vesselle, T. K. Lewellen, W. Eubank, PET-CT image registration in the chest using free-form deformations. *IEEE Trans Med Imaging* **22**, 120-128 (2003).
40. S. Klein, M. Staring, K. Murphy, M. A. Viergever, J. P. Pluim, elastix: a toolbox for intensity-based medical image registration. *IEEE Trans Med Imaging* **29**, 196-205 (2010).
41. R. W. Williams, P. Rakic, Three-dimensional counting: an accurate and direct method to estimate numbers of cells in sectioned material. *J Comp Neurol* **278**, 344-352 (1988).
42. R. M. Deacon, J. N. Rawlins, T-maze alternation in the rodent. *Nat Protoc* **1**, 7-12 (2006).
43. L. Spowart-Manning, F. J. van der Staay, The T-maze continuous alternation task for assessing the effects of putative cognition enhancers in the mouse. *Behav Brain Res* **151**, 37-46 (2004).
44. J. E. Knox *et al*., High resolution data-driven model of the mouse connectome. *bioRxiv*, (2018).